Stability of a jet moving in a rectangular microchannel

M. G. Cabezas
Departmento de Ingeniería Mecánica, Energética y de los Materiales and Instituto de Computación Científica Avanzada (ICCAEx), Universidad de Extremadura, Avda. de Elvas s/n, E-06071 Badajoz, Spain

M. A. Herrada
Escuela Técnica Superior de Ingenieros, Universidad de Sevilla, Avda. de los Descubrimientos s/n, E-41092-Sevilla, Spain

José M. Montanero
Departmento de Ingeniería Mecánica, Energética y de los Materiales and Instituto de Computación Científica Avanzada (ICCAEx), Universidad de Extremadura, Avda. de Elvas s/n, E-06071 Badajoz, Spain

(Received 5 July 2019; published 18 November 2019)

We study numerically the basic flow and linear stability of a capillary jet confined in a rectangular microchannel. We consider both the case where the interface does not touch the solid surfaces and that in which the jet adheres to them with a contact angle slightly smaller than 180°. Given an arbitrary set of values of the governing parameters, the fully developed (parallel) two-dimensional basic flow is calculated and then the growth rate of the dominant perturbation mode is determined as a function of the wave number. The flow is linearly stable if that growth rate is negative for all the wave numbers considered. We show that when the coflowing stream viscosity is sufficiently small in terms of that of the jet, there is an interval of the flow rate ratio Q for which the jet adheres to the walls or not depending on whether the flow is established by decreasing or increasing the value of Q. When the distance between the interface and the channel wall is of the order of the jet radius, the jet is unconditionally unstable. However, for sufficiently small interface-to-wall distances, the viscous stress can dominate the capillary pressure and fully stabilize the flow. Our results suggest that the capillary modes are suppressed and the flow becomes stable when the jet adheres to the channel walls. The combination of the above results indicates that, under certain parametric conditions, stable or unstable jets can be formed depending on whether the experimenter sets the flow rate ratio by decreasing or increasing progressively the jet flow rate while keeping constant that of the outer stream. Our theoretical predictions for the stablity of a coflow in a rectangular channel are consistent with previous experimental results [Humphry *et al.*, Phys. Rev. E **79**, 056310 (2009)].

DOI: 10.1103/PhysRevE.100.053104

I. INTRODUCTION

The stability of confined capillary jets is of great interest at both fundamental and practical levels, especially in channels with noncircular cross sections, which are commonly used in microfluidics [1]. For instance, technologies like those involving high-throughput screening of chemical and biological processes critically rely on the controlled drop formation and manipulation. In addition, stable coflows are more efficient than confined droplet flows to transport fluids over long distances due to the reduction of friction. The confinement of the liquid thread is expected to play a relevant role in the jet breakup both during the growth of the small-amplitude perturbations triggering the process and during the final nonlinear phase of the breakup. An interesting example of this is the droplet-to-string transition taking place in concentrated polymer blends flowing between parallel surfaces when the size of the droplets becomes comparable to the gap width between those surfaces [2].

The capillary instability of a fluid thread has been known for a long time [3]. The pioneering works conducted by Plateau [4] and Rayleigh [5] for jets moving in a passive ambient were generalized by Tomotika [6] for fluid threads surrounded by coflowing viscous streams much wider than those threads. Most theoretical works on the stability of confined capillary jets have considered the circular geometry. Hickox [7] studied analytically the stability of the pressure-driven jet in a tube for infinitely small wave numbers. The flow was found to be unstable under axisymmetric perturbations in all the cases considered [7]. Guillot *et al.* [8] analyzed the convective-to-absolute instability transition in this configuration for low Reynolds numbers. The flow was unstable, and the dripping and jetting experimental realizations approximately corresponded to convective and absolute instability, respectively. Neglecting the angular dependence of the perturbations, Guillot *et al.* [9] examined the linear stability of a jet in a rectangular channel and found that absolute instability was enhanced by the channel corners. Janssen *et al.* [10] studied numerically the growth of small-amplitude varicose perturbations in jets flowing between parallel surfaces. Confinement did not completely stabilize the jet in any of the cases considered.

There are very few configurations where the capillary instability in cylindrical jets can be completely suppressed.

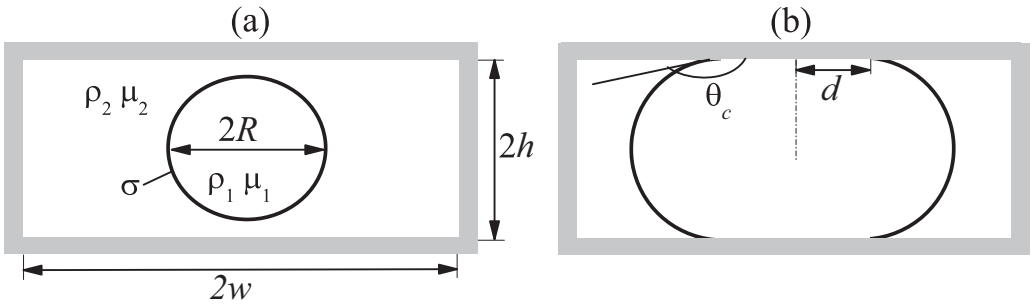

FIG. 1. The two possible configurations depending on whether the jet touches the solid surfaces or not: the nonadhering (a) and the adhering (b) configuration.

The temporal linear stability analysis shows that an external shear flow [11] or the existence of a solid core [12] can produce this effect. When the jet adheres to a solid surface, it forms a rivulet. Rivulets with anchored triple contact lines and contact angles less than 90° can be stabilized by the solid surface [13]. This fact suggests that jets flowing between two parallel surfaces may become stable if they manage to adhere to those surfaces. Using the same approach as that of Hickox [7], Kashid *et al.* [14] found certain parameter conditions for which a jet confined in a circular tube becomes stable under perturbations with infinitely small wave numbers. In principle, this implies that the capillary instability is completely suppressed under those conditions because the damping of perturbations for vanishing wave number is typically a sufficient condition for stability.

Experiments have systematically shown that jets coflowing with other liquids in wide channels [15] or in cylindrical capillaries [16] are unconditionally unstable, the question is whether the nature of that instability is absolute or convective [17]. Cubaud and Mason [18] examined the evolution of threads surrounded by less viscous immiscible liquids in square microchannels. The threads broke up into droplets due to the capillary instability in all the cases considered. The experimental analysis of Geschiere *et al.* [19] suggests that confinement can slow down the growth of capillary perturbations but their complete suppression requires the contact between the jet and at least one of the channel walls.

There have also been experimental realizations where a confined jet seems to remain stable over time and length scales much larger than those characterizing the configuration. Humphry *et al.* [20] and de Saint Vincent *et al.* [21] studied experimentally the stability of a liquid jet coflowing with an immiscible liquid current inside a microfluidic channel whose width was considerably larger than its height. Hydrodynamic instabilities were not observed throughout the channel when the inner liquid width was comparable to or larger than the channel height. In the experiments conducted by Son *et al.* [22], polymeric threads moving between parallel surfaces adopted noncylindrical shapes and were found to be stable for sufficiently small values of the ratio between the channel height and the thread diameter. The step-emulsification in a shallow microchannel shows that the jet can remain stable until it reaches the reservoir, although the small distance between the jet inlet and that reservoir does not allow one to determine whether the former is stable [23].

Despite its relevance, the hydrodynamic linear stability analysis of a liquid capillary jet in a rectangular microchannel has not been carried out yet, probably due to the difficulties associated with the spatial dependence of the base flow over the microchannel cross section. Apparently, the fundamental question of whether the channel can completely suppress the capillary perturbations in a fully developed (parallel) flow has been addressed only by Hickox [7] and Kashid *et al.* [14] for infinitely small wave numbers, who came to different conclusions. On the other hand, experiments cannot give a definitive answer to that question because (i) the fully developed flow condition cannot be easily achieved, (ii) perturbations with very small growth rates are very difficult to detect, and (iii) wetting phenomena cannot be completely ruled out. In fact, submicrometer films can form between a liquid jet and the channel wall when the diameter of the former exceeds the height of the later [24]. The existence of those films or, on the contrary, the adhesion of the jet to the channel cannot be ensured with the image acquisition systems typically used in experiments.

In this work, we will conduct the temporal linear stability analysis of the fully developed flow produced when a pressure-driven jet coflows with a liquid stream in a rectangular microchannel, considering both the nonadhesion and adhesion configurations in which the jet does not touch and slips over the channel wall, respectively. The base flow and its eigenmodes will be calculated numerically for arbitrary values of the governing parameters.

II. BASE FLOW AND LINEAR STABILITY ANALYSIS

A. Formulation of the problem

Consider an infinite jet of radius R, density ρ_1, and viscosity μ_1 moving inside a rectangular channel of width $2w$ and height $2h$ [Case (a) of Fig. 1]. The jet coflows with an outer liquid stream of density ρ_2 and viscosity μ_2. The surface tension of the interface between the two liquids is σ. Because of the jet's submillimeter size, gravity effects are neglected. The flow rates of the inner and outer phases are $Q_1 = A_1 W_1$ and $Q_2 = (4wh - A_1)W_2$, respectively, where A_1 is the jet cross-sectional area, and W_1 and W_2 are the mean velocities in the jet and the outer phase, respectively. We will suppose that the unperturbed flow is fully developed, i.e., parallel to the channel axis and driven by a constant pressure gradient

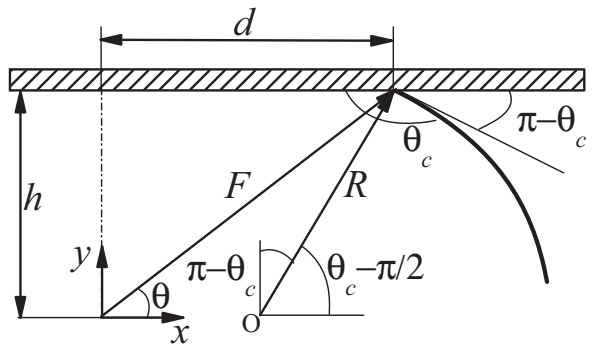

FIG. 2. Sketch of a cross section of the configuration (b) of Fig. 1. R is the radius of curvature of the interface.

$\hat{\mathcal{P}}$. Under these conditions, the interface curvature must be constant. Otherwise, the pressure would not be uniform over the jet and outer stream cross sections, and the velocity field would have nonzero components along that plane. In other words, the existence of a noncircular jet in a rectangular microchannel is not compatible with the condition of fully developed flow.

For large-enough values of the flow rate ratio $Q \equiv Q_1/Q_2$, the jet touches and adheres to the upper and lower channel walls [Case (b) of Fig. 1]. In this case, the liquid-liquid interface forms a contact angle θ_c with the wall at a distance d from the vertical symmetry plane (Fig. 2). We will restrict ourselves to $\theta_c \geqslant \pi/2$ because the inner phase does not wet the channel walls in most microfluidic experiments. As in the nonadhesion configuration, we will assume fully developed flow with a constant interface radius of curvature R. As discussed by Dussan [25], the unpertubed contact angle θ_c takes a value within the interval bounded by the receding and advancing contact angles characterizing a real surface. The triple contact line is pinned to the solid surface for contact angles in that interval. Linear perturbations produce infinitesimal variations around θ_c. Therefore, the triple contact line remains still during the evolution of those perturbations as long as there is a finite difference between the receding and advancing contact angles, independently of how small that difference could be. For this reason, we will adopt the triple conctant line anchorage condition in our analysis.

We selected a coordinate system with the z axis parallel to the jet and the origin located at the center of the channel (Fig. 2). When the jet does not touch the channel walls, the velocity $\mathbf{v}^{(j)}(\mathbf{r};t) = U^{(j)}(r,\theta,z;t)\mathbf{e_r} + V^{(j)}(r,\theta,z;t)\mathbf{e}_\theta + W^{(j)}(r,\theta,z;t)\mathbf{e_z}$ and pressure $P^{(j)}(r,\theta,z;t)$ fields are described in terms of the cylindrical coordinate system $(\mathbf{e_r}, \mathbf{e}_\theta, \mathbf{e_z})$. Hereafter, the superscripts $j = 1$ and 2 refer to the jet and coflowing stream domains, respectively. In the adhering configuration, the problem is formulated in terms of a Cartesian coordinate system, which is more convenient for numerical purposes. For the sake of brevity, in the next section we write the equations only in the cylindrical coordinate system. The interface location is given by the function $F(\theta,z;t)$, which measures the distance between a surface element and the z axis (Fig. 2).

B. Governing equations

In what follows, all the quantities are made dimensionless using h, W_1, and $\rho_1 W_1^2$ as the characteristic length, velocity, and pressure, respectively. Consequently, we define the channel aspect ratio $\omega \equiv w/h$, the density and viscosity ratios $\rho \equiv \rho_2/\rho_1$, $\mu \equiv \mu_2/\mu_1$, the Reynolds and Weber numbers $\mathrm{Re} \equiv \rho_1 W_1 h/\mu_1$ and $\mathrm{We} \equiv \rho_1 W_1^2 h/\sigma$, the dimensionless radius $\mathcal{R} \equiv R/h$, and triple contact line position $\delta \equiv d/h$.

The velocity and pressure fields are calculated from of the (incompressible) Navier-Stokes equations

$$\frac{[rU^{(j)}]_r}{r} + \frac{V_\theta^{(j)}}{r} + W_z^{(j)} = 0, \tag{1}$$

$$\rho^{\Delta_{j2}}\left[U_t^{(j)} + U^{(j)}U_r^{(j)} + \frac{V^{(j)}}{r}U_\theta^{(j)} + W^{(j)}U_z^{(j)} - \frac{V^{(j)2}}{r}\right] = -P_r^{(j)} + \frac{\mu^{\Delta_{j2}}}{\mathrm{Re}}\left\{\frac{\left[rU_r^{(j)}\right]_r}{r} + \frac{U_{\theta\theta}^{(j)}}{r^2} + U_{zz}^{(j)} - \frac{U^{(j)}}{r^2} - \frac{2V_\theta^{(j)}}{r^2}\right\}, \tag{2}$$

$$\rho^{\Delta_{j2}}\left[V_t^{(j)} + U^{(j)}V_r^{(j)} + \frac{V^{(j)}}{r}V_\theta^{(j)} + W^{(j)}V_z^{(j)} + \frac{U^{(j)}V^{(j)}}{r}\right] = -\frac{P_\theta^{(j)}}{r} + \frac{\mu^{\Delta_{j2}}}{\mathrm{Re}}\left\{\frac{\left[rV_r^{(j)}\right]_r}{r} + \frac{V_{\theta\theta}^{(j)}}{r^2} + V_{zz}^{(j)} - \frac{V^{(j)}}{r^2} + \frac{2U_\theta^{(j)}}{r^2}\right\}, \tag{3}$$

$$\rho^{\Delta_{j2}}\left[W_t^{(j)} + U^{(j)}W_r^{(j)} + \frac{V^{(j)}}{r}W_\theta^{(j)} + W^{(j)}W_z^{(j)}\right] = -P_z^{(j)} + \frac{\mu^{\Delta_{j2}}}{\mathrm{Re}}\left\{\frac{\left[rW_r^{(j)}\right]_r}{r} + \frac{W_{\theta\theta}^{(j)}}{r^2} + W_{zz}^{(j)}\right\}, \tag{4}$$

where Δ_{ij} is the Kronecker delta and the subscripts denote the partial derivative with respect to the corresponding variable. Equations (1)–(4) are integrated considering the kinematic compatibility condition

$$F_t - U^{(j)} + \frac{F_\theta}{F}V^{(j)} + F_z W^{(j)} = 0, \tag{5}$$

and the equilibrium of both normal and tangential stresses,

$$P^{(1)} + \mathbf{n}\cdot\boldsymbol{\tau}^{(1)}\cdot\mathbf{n} = P^{(2)} + \mathbf{n}\cdot\boldsymbol{\tau}^{(2)}\cdot\mathbf{n} + \mathrm{We}^{-1}\boldsymbol{\nabla}\cdot\mathbf{n}, \tag{6}$$

$$\mathbf{t_1}\cdot\boldsymbol{\tau}^{(1)}\cdot\mathbf{n} = \mathbf{t_1}\cdot\boldsymbol{\tau}^{(2)}\cdot\mathbf{n}, \tag{7}$$

$$\mathbf{t_2}\cdot\boldsymbol{\tau}^{(1)}\cdot\mathbf{n} = \mathbf{t_2}\cdot\boldsymbol{\tau}^{(2)}\cdot\mathbf{n}, \tag{8}$$

at the interface position $r = F(\theta,z;t)$. Here $\boldsymbol{\tau}^{(1)} = \mathrm{Re}^{-1}\boldsymbol{\epsilon}^{(1)}$ and $\boldsymbol{\tau}^{(2)} = \mu\mathrm{Re}^{-1}\boldsymbol{\epsilon}^{(2)}$ stand for the viscous stress tensor evaluated at the jet and coflowing stream sides of the interface, respectively, while $\boldsymbol{\epsilon}^{(1)}$ and $\boldsymbol{\epsilon}^{(2)}$ are the corresponding values of the strain rate tensor. In addition, $\mathbf{n}$, $\mathbf{t_1}$, and $\mathbf{t_2}$ are the normal

and two orthogonal tangential unit vectors with respect to the interface, respectively.

In the adhering configuration, the triple contact lines remain fixed during the evolution of the linear pertubations analyzed in this work, which implies that $F(\theta, z; t) = (1 + \delta^2)^{1/2}$ for $\theta = \pm \arctan(\delta^{-1})$ and any value of z and t. Finally, nonslip and symmetry boundary conditions are prescribed at the two solid surfaces and the planes $\theta = 0$ and $\pi/2$, respectively.

As can be seen, the solution $\{\mathbf{v}^{(j)}(\mathbf{r}; t), P^{(j)}(\mathbf{r}; t), F(\theta, z; t)\}$ of the governing equations is obtained in terms of the dimensionless parameters $\{\omega, \rho, \mu, \mathrm{Re}, \mathrm{We}\}$, and the position δ of the triple contact line in the adhesion case. The formulation of the problem is closed by imposing the dimensionless volume of the inner phase. This volume is univocally determined by $\mathcal{R}$ and $\{\theta_c, \delta\}$ in the nonadhesion and adhesion cases, respectively. The flow rate ratio $Q \equiv Q_1/Q_2$ is a function of the above parameters.

C. Basic flow

The basic solution of the problem described above is the parallel flow given by the expressions $\mathbf{v_0}^{(j)} = W_0^{(j)}(r, \theta)\mathbf{e_z}$ and $P_0^{(j)}(z) = \hat{P}_0^{(j)} - \mathcal{P}z$, where $\hat{P}_0^{(1)} = 1/(\mathcal{R}\mathrm{We})$ and $\hat{P}_0^{(2)} = 0$ are the pressures at the section $z = 0$ on the inner and outer sides of the interface, respectively, and $\mathcal{P} \equiv \hat{\mathcal{P}}/(\rho_1 W_1^2)$ is the dimensionless pressure gradient. The interface contour $F_0(\theta)$ is given by the functions $F_0(\theta) = \mathcal{R}$ and

$$F_0(\theta) = [1 - \delta^2 - 2\delta\tan\theta_c + (\delta + \tan\theta_c)^2\cos^2\theta]^{1/2} + (\delta + \tan\theta_c)\cos\theta \tag{9}$$

in the nonadhesion and adhesion cases, respectively. The functions $W_0^{(j)}(r, \theta)$ verify the Poisson equations

$$-\mathcal{P}\mathrm{Re} = \mu^{\Delta_{j2}}\left\{\frac{[rW_{0r}^{(j)}]_r}{r} + \frac{W_{0\theta\theta}^{(j)}}{r^2}\right\} \tag{10}$$

for the jet and coflowing stream domains. Both the velocity and tangential stresses are continuous functions across the interface, i.e.,

$$W_0^{(1)}(F_0, \theta) = W_0^{(2)}(F_0, \theta), \tag{11}$$

$$a^{-1}W_{0r}^{(1)}(F_0, \theta) + b(aF_0)^{-1}W_{0\theta}^{(1)}(F_0, \theta) = \mu\left[a^{-1}W_{0r}^{(2)}(F_0, \theta) + b(aF_0)^{-1}W_{0\theta}^{(2)}(F_0, \theta)\right], \tag{12}$$

where $a = \sqrt{1 + b^2}$, $b = -F_0'/F_0$, and the prime denotes the derivative with respect to θ. Finally, the nonslip boundary condition is prescribed at the solid walls, while the velocity is a symmetric function with respect to the planes $\theta = 0$ and $\pi/2$.

Once the inner phase volume has been prescribed through either $\mathcal{R}$ or $\{\theta_c, \delta\}$, the product $\mathcal{P}\mathrm{Re}$ in Eq. (10) can be calculated as a function of the aspect and viscosity ratios ω and μ exclusively. Specifically, the value of $\mathcal{P}\mathrm{Re}$ is that leading to an average inner velocity equal to unity. It must be noted that the Weber number only affects the jump of pressure across the interface due to the surface tension, and, therefore, it does not affect the velocity field. In sum, the basic flow can be determined from the numerical integration of the above equations as a function of $\{\omega, \mu, [\mathcal{R} \text{ or } (\theta_c, \delta)]\}$ exclusively. The flow rate ratio Q is a function of those parameters.

One may gain insight into the system behavior by considering the limiting case $\mathcal{R} \to 1$, where the cylindrical interface almost touches the solid wall. In this situation, the limits $\mu \to 0$ and $\mu \to \infty$ deserve special attention. For $\mu \to 0$ [and $W_0^{(2)}(r, \theta)$ finite], Eq. (10) for $j = 2$ yields $-\mathcal{P}\mathrm{Re} \to 0$. Substituting this result into Eq. (10) for $j = 1$ leads to $W_0^{(1)}(r, \theta) \to 1$, which indicates that the jet tends to move as a solid body when its viscosity is much higher than that of the outer phase. Assume that this limit is reached in the way $-\mathcal{P}\mathrm{Re} \to \mathcal{C}\mu$, where $\mathcal{C}$ is a function of the aspect ratio ω. Considering again Eq. (10) for $j = 2$, one concludes that the outer velocity field corresponds to a Poiseuille-Couette flow driven by both the effective pressure gradient $\mathcal{C}(\omega)$ and the drag exerted by the inner jet, which moves as a solid body in this limit. In this scenario, one expects the flow rate ratio Q to become a function of the aspect ratio ω exclusively. However, a jet approaching the wall while moving as a solid body would make the viscous stress diverge in the gap enclosed by the jet and the wall because the outer stream velocity would have to evolve from 1 at the interface to 0 at the solid wall within a vanishing distance. For this reason, the jet velocity in the vicinity of the wall must decrease as $\mathcal{R} \to 1$, no matter how large the inner viscosity is. This effect makes Q decrease in the limit $\mathcal{R} \to 1$ for any finite value of μ. We will describe this effect in more detail from the numerical solution in Sec. III A.

Equation (10) can be rewritten as

$$\left\{\frac{[rW_{0r}^{(1)}]_r}{r} + \frac{W_{0\theta\theta}^{(1)}}{r^2}\right\} = \mu\left\{\frac{[rW_{0r}^{(2)}]_r}{r} + \frac{W_{0\theta\theta}^{(2)}}{r^2}\right\}. \tag{13}$$

For $\mu \to \infty$ [and $W_0^{(1)}(r, \theta)$ finite], Eq. (13) together with the nonslip boundary condition at the solid wall yield $W_0^{(2)}(r, \theta) \to 0$, which indicates that the outer phase behaves a solid wall at rest. In this case, the inner velocity field tends to the cylindrical Poiseuille flow powered by the pressure gradient $-\mathcal{P}\mathrm{Re} = 8$, where we have taken into account that the average inner velocity equals unity. Substituting this result into Eq. (10) for $j = 2$ leads to $W_0^{(2)}(r, \theta) \propto \mu^{-1}$, which implies that $Q \to f(\omega)\mu$ in this limit. The validity of this asymptotic analysis will be confirmed by the numerical simulations.

D. Temporal linear stability analysis

In order to study the stability of the basic flow described in the previous section, we consider the infinitesimal perturbations defined by the following expression:

$$\begin{bmatrix} U^{(j)}(r, \theta, z; t) \\ V^{(j)}(r, \theta, z; t) \\ W^{(j)}(r, \theta, z; t) \\ P^{(j)}(r, \theta, z; t) \\ F(\theta, z; t) \end{bmatrix} = \begin{bmatrix} 0 \\ 0 \\ W_0^{(j)}(r, \theta) \\ P_0^{(j)}(z) \\ F_0(\theta) \end{bmatrix} + \begin{bmatrix} u^{(j)}(r, \theta) \\ v^{(j)}(r, \theta) \\ w^{(j)}(r, \theta) \\ p^{(j)}(r, \theta) \\ F_0(\theta)f(\theta) \end{bmatrix} \times \exp[i(kz - \Omega t)], \tag{14}$$

where k and $\Omega = \Omega_r + i\Omega_i$ are the axial (real) wave number and frequency, respectively. The unit vector normal to the

interface is perturbed accordingly:

$$\mathbf{n} = \mathbf{n}_0 + \tilde{\mathbf{n}}, \quad \tilde{\mathbf{n}} = \mathbf{n}^* \exp[i(kz - \Omega t)],$$
$$\mathbf{n}^* = \left(\frac{bf'}{a^3}\mathbf{e_r} - \frac{f'}{a^3}\mathbf{e}_\theta - \frac{fikF_0}{a}\mathbf{e_z}\right), \tag{15}$$

where $\mathbf{n}_0$ is the unit vector perpendicular to the unperturbed interface shape.

If one introduces Eq. (14) into the incompressible Navier-Stokes equations (1)–(4), and neglects nonlinear terms, then the result is

$$ikw^{(j)} + v_\theta^{(j)}/r + [ru^{(j)}]_r/r = 0, \tag{16}$$

$$\Omega^{*(j)}u^{(j)} + \rho^{-\Delta_{j2}}p_r^{(j)} - \left(\frac{\mu}{\rho}\right)^{\Delta_{j2}}\frac{1}{\mathrm{Re}}\left[\hat{\nabla}^2 u^{(j)} - \frac{u^{(j)}}{r^2} - \frac{2}{r^2}v_\theta^{(j)}\right] = 0, \tag{17}$$

$$\Omega^{*(j)}v^{(j)} + \rho^{-\Delta_{j2}}\frac{1}{r}p_\theta^{(j)} - \left(\frac{\mu}{\rho}\right)^{\Delta_{j2}}\frac{1}{\mathrm{Re}}\left[\hat{\nabla}^2 v^{(j)} - \frac{v^{(j)}}{r^2} + \frac{2}{r^2}u_\theta^{(j)}\right] = 0, \tag{18}$$

$$\Omega^{*(j)}w^{(j)} + W_{0r}^{(j)}u^{(j)} + \frac{1}{r}W_{0\theta}^{(j)}v^{(j)} + \rho^{-\Delta_{j2}}ikp^{(j)} - \left(\frac{\mu}{\rho}\right)^{\Delta_{j2}}\frac{1}{\mathrm{Re}}\hat{\nabla}^2 w^{(j)} = 0, \tag{19}$$

where $\Omega^{*(j)} = [-i\Omega + ikW_0^{(j)}]$, $\hat{\nabla}^2 = \partial^2/\partial r^2 + r^{-1}\partial/\partial r - k^2 + r^{-2}\partial^2/\partial\theta^2$.

Equations (16)–(19) must be solved subject to the following boundary conditions. At the unperturbed interface position $r = F_0(\theta)$, the kinematic compatibility condition verifies

$$i\Omega f F_0 - ikfF_0 W_0^{(1)} + u^{(1)} = 0, \tag{20}$$

the velocity field is continuous,

$$u^{(1)} = u^{(2)}, \quad v^{(1)} = v^{(2)}, \quad w^{(1)} + F_0 f W_{0r}^{(1)} = w^{(2)} + F_0 f W_{0r}^{(2)}, \tag{21}$$

and the stresses on both sides of the interface are balanced,

$$\tau_{t1}^{(1)} = \mu\tau_{t1}^{(2)}, \quad \tau_{t2}^{(1)} = \mu\tau_{t2}^{(2)}, \quad p^{(1)} - p^{(2)} - \mathrm{Re}^{-1}\left[\tau_n^{(1)} - \mu\tau_n^{(2)}\right] = \mathrm{We}^{-1}\nabla\cdot\mathbf{n}^*, \tag{22}$$

$$\tau_{t1}^{(j)} = \frac{1}{F_0^3 a^2}\left[a_1 v^{(j)} - 2F_0F_0'v_\theta^{(j)} - a_1F_0v_r^{(j)} + 2F_0^2F_0'u_r^{(j)} - a_1u_\theta^{(j)} - 2F_0F_0'u - ikfaa_3\right], \tag{23}$$

$$\tau_{t2}^{(j)} = \frac{1}{F_0^4 a^3}\left[-F_0'a_2w_\theta^{(j)} + a_2F_0^2w_r^{(j)} + F_0^2a_2iku^{(j)} - F_0F_0'a_2ikv^{(j)} + fa_4 - f'a_3\right], \tag{24}$$

$$\tau_n^{(j)} = \frac{2}{F_0^3 a^2}\left[F_0F_0'v^{(j)} + F_0'^2v_\theta^{(j)} - F_0^2F_0'v_r^{(j)} + F_0'^2u^{(j)} - F_0'F_0u_\theta^{(j)} + F_0^3u_r^{(j)} + ikafa_5\right], \tag{25}$$

$$a_1 = \left(F_0'^2 - F_0^2\right), \quad a_2 = (F_0'^2 + F_0^2), \quad a_3 = F_0^3\left(W_{0\theta} + F_0'W_{0r}\right), \tag{26}$$

$$a_4 = a_2\left(F_0'W_{0\theta} - F_0F_0'W_{0r\theta} + F_0^3W_{0rr}\right), \quad a_5 = F_0^2\left(F_0'W_{0\theta} - F_0^2W_{0r}\right), \tag{27}$$

$$\nabla\cdot\mathbf{n}^* = -\frac{f}{F_0aa_2}\left(2F_0'^2 + F_0^2 - a_2F_0^2k^2 - F_0F_0''\right) - \frac{f'}{aa_2^2F_0}\left(F_0^3F_0' + 4F_0'^3F_0\right) - 3F_0^2F_0'F_0'' - \frac{f''F_0}{aa_2}. \tag{28}$$

The anchorage $f = 0$ and nonslip $u^{(j)} = v^{(j)} = w^{(j)} = 0$ boundary conditions are imposed at the solid walls and the triple contact lines, respectively.

The solution of the temporal linear stability analysis is obtained in terms of the set of parameters $\{\omega, \rho, \mu, \mathrm{Re}, \mathrm{We}, [\mathcal{R} \text{ or } (\theta_c, \delta)]\}$. As can be observed, the density ratio, as well as the Reynolds and Weber numbers, come into play essentially due to the fluid particle acceleration and capillary pressure variation arising in the perturbation. To carry out the stability analysis, the basic flow is calculated by solving the Poisson equations (10) with the corresponding boundary conditions. This solution is used in the linearized problem to get a homogeneous system of equations whose solvability condition leads to the dispersion relation $D(k, \Omega) = 0$. The solutions of this relation for a given wave number k are the eigenfrequencies of the corresponding modes. There are infinite modes for a given choice of the governing parameters. The dominant mode is that with the largest value of Ω_i. If the dominant growth rate is positive for some value of k, then the system is linearly unstable.

Both the basic flow and linear perturbations are calculated numerically. To reduce the computing time, we only consider a quarter of the channel section and impose symmetry conditions on the horizontal and vertical midplanes. Therefore, instabilities that do not exhibit this symmetry are not taken into account. The jet and coflowing stream domains are mapped onto fixed quadrangular domains through a coordinate transformation. The equations are discretized in the radial direction by expanding the fields in terms of truncated Chebyshev series [26]. The angular derivatives were calculated with fourth-order central finite differences using uniformly distributed points. Both the fluid domain mapping and the spectral

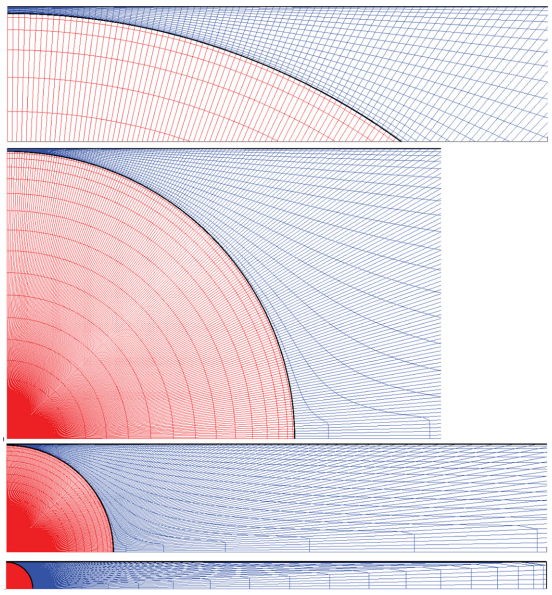

FIG. 3. Details of the grid used in one of the cases considered in this work.

discretization accumulate the grid points in the vicinity of the free surface and solid walls, where larger gradients of the hydrodynamic fields are expected. This discretization method allows one to get very accurate results with a reduced number of grid points. More details of the numerical method can be found in Ref. [27]. We verified that neither the basic flow nor its eigenmodes significantly changed when the number of grid points was considerably increased. Specifically, when the number of grid points was doubled in the nonadhering configuration, the variation of the growth rate was smaller than 1% in most cases. This variation increased up to values slightly smaller than 7% for $10^{-5} \lesssim \Omega_i \lesssim 10^{-3}$. When the number of grid points was multiplied by a factor 1.5 in the adhering configuration, the variation of the growth rate was smaller than 5% in most cases. Figure 3 shows the grid used to analyze one of the cases considered in this work.

III. RESULTS

A. The basic flow

In this section, we study the basic flow in both the nonadhering and adhering configurations. In the latter case, and given the large dimension of the parameter space, we will restrict ourselves to nonwetting conditions ($\theta_c \simeq 180^\circ$) commonly observed in experimental realizations. Following Humphry *et al.* [20], we will consider in Figs. 4–6 a large value of the aspect ratio ω. Figure 4 shows the velocity isocontours for both a nonadhesion case and an adhesion configuration. Given the large value of the jet viscosity as compared with that of the outer stream, the jet acts like a solid wall splitting the channel into two parts. In each of those two parts, the velocity field corresponds approximately to the Poiseuille flow in a rectangular channel because the jet velocity is much smaller than that of the coflowing current. When the jet touches the wall, the velocity decreases next to the wall and at the interface around $y = 0$.

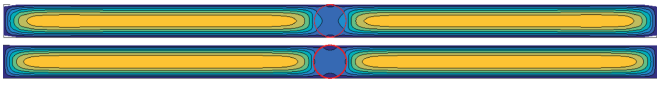

FIG. 4. Velocity isocontours for the nonadhesion case with $\mathcal{R} = 0.99$ (upper graph) and the adhesion configuration with $\delta = 0.01$ and $\theta_c = 179.99^\circ$ (lower graph). The red circle corresponds to the interface. In both cases, the aspect and viscosity ratios are $\omega = 20$ and $\mu = 0.08$.

Figure 5 shows the dependence of the flow rate ratio Q with respect to the jet radius $\mathcal{R}$ and the triple contact line position δ in the nonadhering and adhering configurations, respectively. We consider a moderately large value of μ in Fig. 5(a). In this case, one observes the expected simple behavior: The flow rate ratio Q increases monotonously with $\mathcal{R}$ and δ due to the increase of the jet cross-sectional area. The transition from the adhesion to the nonadhesion configuration takes place at the critical flow rate ratio Q^*.

In Fig. 5(b), we analyze what occurs for a small value of the viscosity ratio μ. The left side of the figure shows the viscosity effect anticipated in the asymptotic analysis for $\mathcal{R} \to 1$ and $\mu \to 0$ (see Sec. II C). The jet moves approximately like a solid body because its viscosity is much higher than that of the outer phase. The flow rate ratio Q increases with $\mathcal{R}$ for $\mathcal{R} < 0.85$ due to the increase of the jet cross-sectional area. For $\mathcal{R} > 0.85$, viscous stresses in the thin fluid layer located between the jet and the wall blow up because the outer stream velocity has to evolve from 1 at the interface to 0 at the wall within a vanishing distance. These stresses manage to curb the jet in that region in spite of its large viscosity. As a consequence, the inner flow rate (and therefore Q) slightly decreases as $\mathcal{R}$ increases even though the jet cross-sectional area continues increasing. We denote by $Q_{\max}$ the maximum flow rate ratio that can be reached in the nonadhering configuration. The flow rate $Q_{\max}$ can be exceeded in the adhering configuration for sufficiently large values of the triple contact line position δ. The value Q^* is the critical flow rate ratio for which the jet adheres to the wall, i.e., for which the jet becomes tangent to the wall ($\mathcal{R} = 1$). Interestingly, two jet radii are compatible with the prescribed value of Q in the interval between Q^* and $Q_{\max}$, which prevents one from using Q as a control parameter in a strict sense. In the adhesion configuration, one observes a similar effect to that described above for the free evolving jet. As δ decreases, the inner flow rate decreases down to its minimum value $Q_{\min}$ due to the reduction of the jet cross-sectional area. However, the friction force exerted by the wall on the inner phase decreases with δ. For $\delta < 0.1$, the second effect overcomes the first, and the flow rate transported by the jet slightly increases as δ decreases. The triple contact line position becomes a multivalued function of the flow rate ratio for small values of δ, and, therefore, Q cannot be used as a control parameter in this case either. We finally conclude that

(a) For $Q < Q_{\min}$, the jet cannot touch the channel walls

(b) For $Q > Q_{\max}$, the jet necessarily adheres to those walls

(c) For $Q_{\min} < Q < Q_{\max}$, the system may adopt a state or another depending on whether the basic flow was reached by decreasing or increasing Q (hysteresis effect).

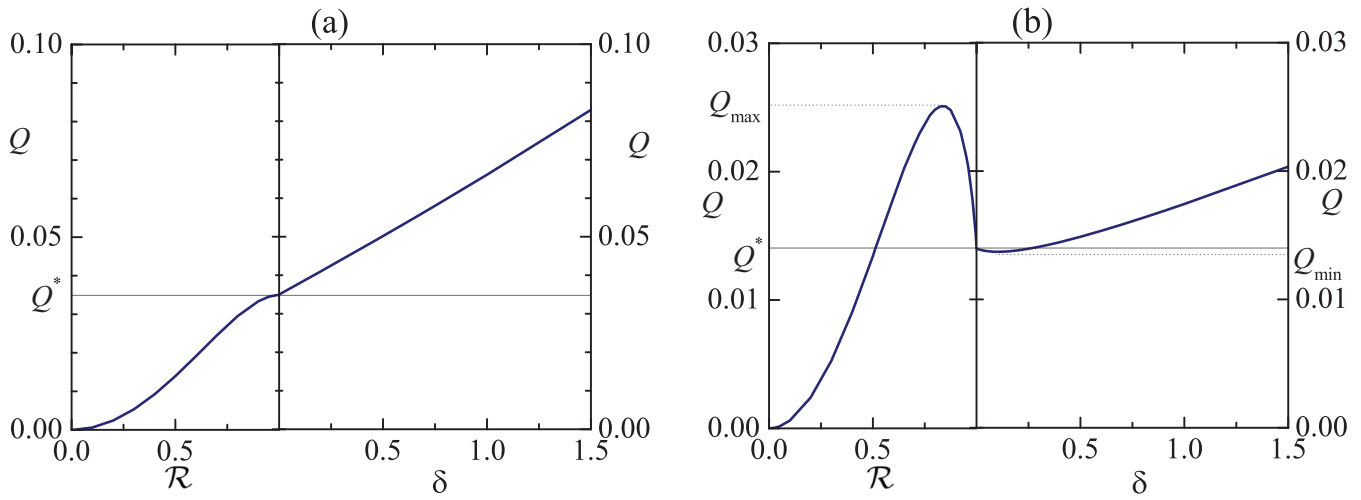

FIG. 5. Flow rate ratio Q as a function of the jet radius $\mathcal{R}$ for the nonadhesion case (a) and the triple contact line position δ for the adhesion configuration (b). In the latter case, $\theta_c = 179.99°$. The viscosity ratios are $\mu = 0.5$ (a) and 0.08 (b). In both cases, the aspect ratio is $\omega = 20$.

To better explain the nonmonotonous behavior of the curves $Q(\mathcal{R})$ and $Q(\delta)$ observed for small values of μ [Fig. 5(b)], we plot in Fig. 6 the velocity profiles along the horizontal and vertical symmetry planes for the viscosity and aspect ratios considered in Fig. 5(b). These profiles have been made dimensionless using the characteristic velocity $W_{1c} = \hat{\mathcal{P}}h^2/\mu_1$. In this way, one can analyze the effect of increasing the jet cross-sectional area while keeping the magnitude of the driving force. Figure 6(a) shows the results for the nonadhering case with $\mathcal{R} = 0.9$ and 0.99. As can be observed, the jet velocity profile significantly decreases when $\mathcal{R}$ slightly increases due to the sharp increase of the viscous stresses in the gap between the jet and the wall channel. The percentage reduction of the outer stream velocity is much smaller (the velocity profile hardly changes for $x \gtrsim 5$), and, therefore, the flow rate ratio $Q = Q_1/Q_2$ decreases despite the increase of the jet cross-sectional area. A similar phenomenon occurs when the jet adheres to the channel wall [Fig. 6(b)] and δ increases from 0.1 to 0.01.

Figure 7 shows the "phase diagram" of the fluid system analyzed in this work. The curves $Q^*(\omega, \mu)$ of the transitional flow rate ratio have been obtained by setting $\mathcal{R} = 0.99995$ for the nonadhesion case. We have verified that the results practically coincide with those calculated by setting $\delta = 0.0001$ in the adhesion configuration. As predicted by the asymptotic analysis (see Sec. II C), $Q^* \to f(\omega)\mu$ for large-enough values of μ. The figure also shows the maximum and minimum flow rate ratios, $Q_{\max}(\omega, \mu)$ and $Q_{\min}(\omega, \mu)$, for the nonadhesion and adhesion cases, respectively. These curves merge with those of the transitional flow rate ratio, $Q^*(\omega, \mu)$, for sufficiently large values of μ. The interval length $Q_{\max} - Q_{\min}$ increases as the channel aspect ratio increases and the viscosity ratio decreases. The curves $Q_{\max}(\omega, \mu)$ correspond to the simple scenario expected where the viscosity effects described above (Fig. 5) are not considered. In this case, $Q_{\max}$ becomes independent from μ in the limit $\mu \to 0$, as predicted by the asymptotic analysis in Sec. II C.

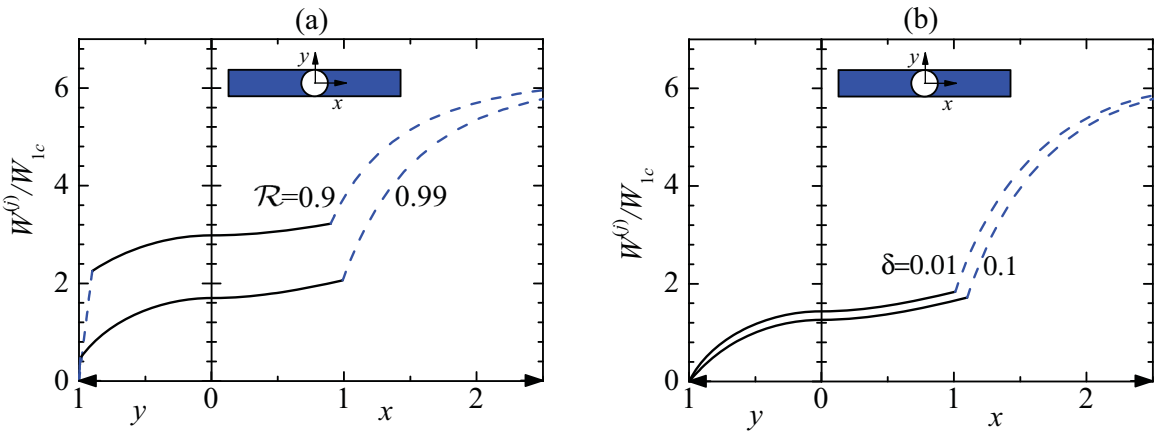

FIG. 6. Velocity profiles along the x and y axes both inside the jet (black solid lines) and in the outer stream (blue dashed lines). The graphs (a) and (b) correspond to nonadhering and adhering configurations, respectively. The viscosity and aspect ratios are $\mu = 0.08$ and $\omega = 20$, respectively. In graph (b), $\theta_c = 179.99°$.

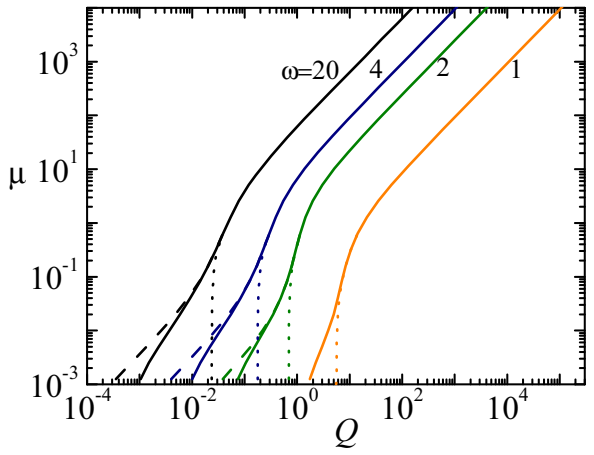

FIG. 7. Phase diagram of the fluid system analyzed in this work. The solid lines are the boundaries $Q^*(\omega, \mu)$ separating the nonadhering and adhering configurations. The dotted and dashed lines correspond to the maximum and minimum flow rate ratios, $Q_{\max}(\omega, \mu)$ and $Q_{\min}(\omega, \mu)$, for the nonadhesion and adhesion cases, respectively. The labels indicate the values of ω. The results were obtained for $\theta_c = 179.99^\circ$.

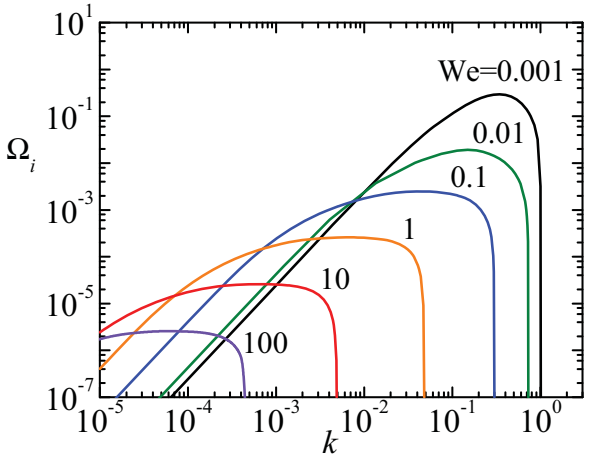

FIG. 8. Growth rate Ω_i of the dominant mode as function of the wave number k for different values of We. The values of the rest of governing parameters are $\{\omega = 20,\ \rho = 1,\ \mu = 0.32,\ \mathrm{Re} = 0.1,\ \mathcal{R} = 0.99\}$.

As mentioned above, the jet cannot touch the channel walls for $Q < Q_{\min}(\omega, \mu)$, while it necessarily adheres to them for $Q > Q_{\max}(\omega, \mu)$ (see Fig. 5). The results presented in the next section indicate that the jet is linearly stable if it touches the channel walls. Therefore, $Q > Q_{\max}(\omega, \mu)$ is a sufficient condition for the linear stability of confined jets. In addition, our results will show that cylindrical jets are generally unstable, although they may stabilize as the interface approaches the wall.

B. Linear stability

1. Non-adhering configuration

In this section, we analyze the stability of the nonadhering configuration, where the jet does not touch the channel. For sufficiently large distances between the interface and the channel walls, the jet is expected to be unstable for small-enough wave numbers. As the jet-to-channel distance decreases, a thin liquid layer is trapped between the wall and the interface. The viscous stresses arising in that layer during the growth of the perturbation are expected to stabilize the fluid configuration. For this reason, we will focus on the most interesting case in which the jet almost touches the channel wall ($\mathcal{R} = 0.99$). Figure 8 shows the dependence of the growth rate Ω_i of the dominant perturbation on the Weber number for a fixed value of the Reynolds number. As the Weber number increases, the jet Ohnesorge number $\mathrm{Oh} = \mathrm{We}^{1/2}/\mathrm{Re}$ increases, and the viscous force becomes more important as compared with both inertial and the capillary forces. As a consequence, the flow stabilizes, i.e., the range of unstable wave numbers, the maximum growth rate and the corresponding wave number decrease. The curves for the smaller Weber numbers indicate that the growth rate scales as k^2 for $k \to 0$. This asymptotic law is reached for smaller values of k as the Weber number increases. For a fixed value of k, Ω_i does not exhibit a monotonic dependence with respect to the Weber number. Viscosity does not manage to completely suppress the capillary instability even for the largest (smallest) Weber number (surface tension) value considered.

Figure 9 shows similar behavior to that described above. The dominant growth rate decreases as the Reynolds number decreases for a fixed value of the Weber number due to the stabilizing role played by the jet viscosity. Interestingly, the range of unstable wave numbers does not monotonically decrease as the Reynolds number decreases, which means that viscosity can destabilize certain capillary modes despite its dissipative character. For instance, perturbations with $k \simeq 0.1$ become unstable when the Reynolds number decreases from 100 to 10. This means that instability arises for these wave numbers if both the jet and outer stream viscosities increase by a factor of 10. This counterintuitive behavior resembles what

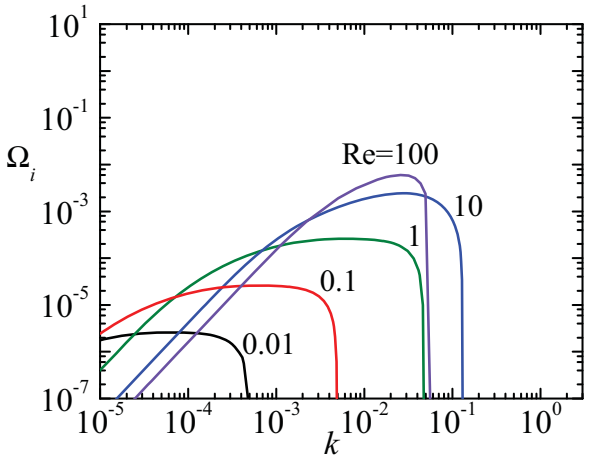

FIG. 9. Growth rate Ω_i of the dominant mode as function of the wave number k for different values of Re. The values of the rest of governing parameters are $\{\omega = 20,\ \rho = 1,\ \mu = 0.32,\ \mathrm{We} = 10,\ \mathcal{R} = 0.99\}$.

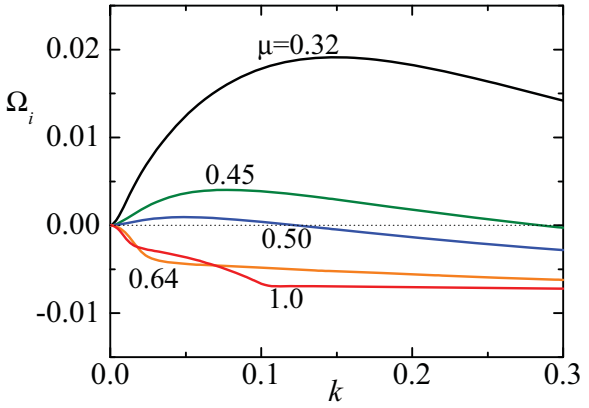

FIG. 10. Growth rate Ω_i of the dominant mode as function of the wave number k for different values of μ. The values of the rest of governing parameters are $\{\omega = 20, \rho = 1, \mathrm{Re} = 0.1, \mathrm{We} = 0.01, \mathcal{R} = 0.99\}$.

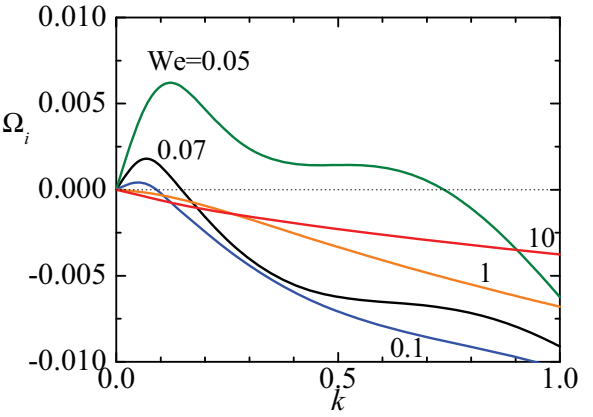

FIG. 12. Growth rate Ω_i of the dominant mode as function of the wave number k for different values of We. The values of the rest of governing parameters are $\{\omega = 20, \rho = 1, \mu = 0.51, \mathrm{Re} = 1, \mathcal{R} = 0.99\}$.

happens in gaseous rivulets coflowing with liquid streams in microchannels [13].

A natural question is whether the capillary instability can be *completely* suppressed by viscous stresses in the nonadhering case, which implies $\Omega_i < 0$ for all wave numbers. As mentioned above, the wave number corresponding to the maximum growth rate decreases as the system stabilizes. Therefore, that question reduces to determining whether $\partial\Omega_i/\partial k|_{k=0}$ becomes negative in some regions of the parameter space. Unfortunately, our numerical approach cannot directly address this problem. We can only infer the value of $\partial\Omega_i/\partial k|_{k=0}$ from a discrete set of Ω_i values calculated for small k. We have explored the parameter space and have found conditions under which the jet seems to be stable under infinitesimal perturbations. For instance, the results in Fig. 10 suggest that the jet fully stabilizes for some value of the viscosity ratio μ between 0.5 and 0.64. The viscous stress in the liquid layer trapped between the jet and the channel wall manages to eliminate the capillary instability for large-enough outer stream viscosities. As mentioned above, we only plot the growth rate of the dominant mode for a given choice of the governing parameters. The discontinuity of $\partial\Omega_i/\partial k$ for $\mu = 1$ corresponds to a crossover of different modes. In other words, it corresponds to a value of k for which the dominant mode changes.

The capillary instability is also eliminated if the Reynolds number is decreased while keeping constant the viscosity ratio (Fig. 11); in other words, if the two viscosities take large-enough values. Specifically, the results shown in Fig. 11 indicate that all the small-amplitude perturbations are damped by viscosity for Reynolds numbers smaller than some value between 0.1 and 1. As mentioned above, viscosity dominates surface tension for large-enough Ohnesorge numbers. Therefore, one can expect the jet to become stable under capillary perturbations for sufficiently large values of that dimensionless parameter. This effect is also observed in Fig. 12, which shows the complete suppression of the capillary instability when the Weber number is increased while keeping the Reynolds number constant.

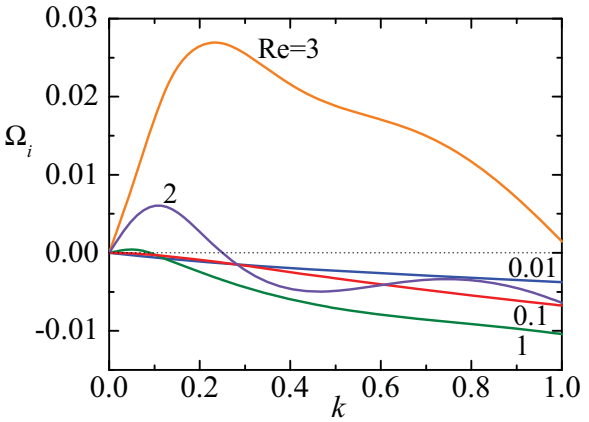

FIG. 11. Growth rate Ω_i of the dominant mode as function of the wave number k for different values of Re. The values of the rest of governing parameters are $\{\omega = 20, \rho = 1, \mu = 0.51, \mathrm{We} = 0.1, \mathcal{R} = 0.99\}$.

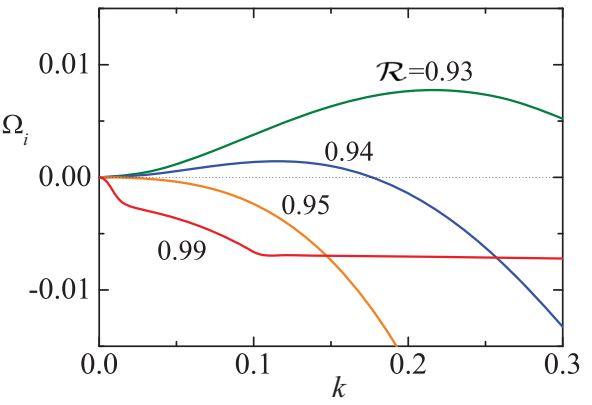

FIG. 13. Growth rate Ω_i of the dominant mode as function of the wave number k for different values of $\mathcal{R}$. The values of the rest of governing parameters are $\{\omega = 20, \rho = 1, \mu = 1, \mathrm{Re} = 0.1, \mathrm{We} = 0.01\}$.

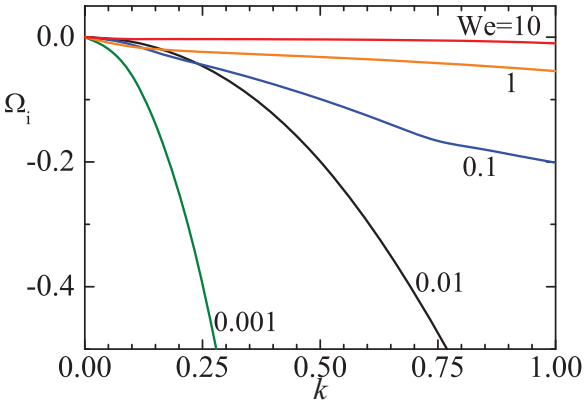

FIG. 14. Growth rate Ω_i of the dominant mode as function of the wave number k for different values of We. The values of the rest of governing parameters are $\{\omega = 20,\ \rho = 1,\ \mu = 0.32,\ \mathrm{Re} = 0.1,\ \delta = 0.21,\ \theta_c = 170^\circ\}$.

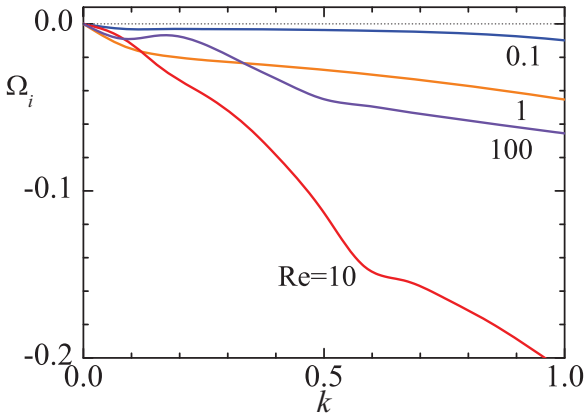

FIG. 15. Growth rate Ω_i of the dominant mode as function of the wave number k for different values of Re. The values of the rest of governing parameters are $\{\omega = 20,\ \rho = 1,\ \mu = 0.32,\ \mathrm{We} = 10,\ \delta = 0.21,\ \theta_c = 170^\circ\}$.

The critical influence of the jet-to-wall distance on the system stability is shown in Fig. 13. The range of unstable wave numbers, the maximum growth rate and the corresponding wave number decrease as the gap between the jet and the channel becomes thinner. Apparently, there is a value in the interval $0.94 < \mathcal{R} < 0.95$ beyond which the capillary instability is fully suppressed. As mentioned above, the discontinuity of $\partial\Omega_i/\partial k$ for $\mathcal{R} = 0.99$ corresponds to a crossover of different modes.

The major conclusion of the analysis presented in this section is that rectangular channels can fully eliminate the capillary linear instability of liquid jets coflowing with liquid streams for sufficiently small jet-to-wall distances and large-enough Ohnesorge number values. This effect is enhanced when the outer-to-inner viscosity ratio increases. Stabilization can be reached even for moderately small Ohnesorge numbers and viscosity ratios. For instance, Figs. 10–13 show stability for values of those parameters of order unity. In principle, it could be possible to form liquid jets that travel along a microfluidic channel, as long as it wishes, without breaking up into droplets. Humphry *et al.* [20] conducted experiments that showed this possibility. Hickox [7] obtained a similar result for jets confined in circular ducts.

2. *Adhering configuration*

In this section, we study the stability of jets slipping over the channel walls. As occurs with rivulets, the contact between the jet and the wall must hinder the growth of capillary perturbations due to both the reduction of the interface area and the increase of viscous dissipation because of the friction between the jet and the wall. For this reason, we search for critical conditions by focusing our study on relatively small values of the contact length δ and large values of the contact angle θ_c. Figures 14 and 15 show the growth rates calculated for different Weber and Reynolds numbers, respectively. As can be observed, all the cases analyzed are stable. The analysis of the rest of the cases considered led to the same conclusion, which suggests that the adhesion of the jet to the wall completely suppresses the growth of capillary modes. Of course, we cannot categorically state that adhesion is a sufficient condition for stability. Given the large dimension of the parameter space, there could be conditions leading to the destabilization of an adhering jet.

The cases analyzed in Figs. 14 and 15 correspond to the same flow rate ratio $Q = 0.29$ as that considered in Figs. 8

TABLE I. Results for the experimental realizations shown in Figs. 4 and 5 of Ref. [20]. The column "Observation" indicates the experimental observation (Stable = stable jet, Unstable = jet breaking into drops downstream). The column Q^* corresponds to the critical flow rate above which the jet adheres to the wall for the experimental values of ω and μ. The column "Result" indicates the result of the linear stability analysis.

Figure	ω	μ	Q	Observation	Q^*	$\mathcal{R}$	Re	We	Result
4a-h1	19.4	5.3	0.2	Stable	0.126	Adhesion	—	—	Stable
4b-h1	19.4	5.3	0.4	Stable	0.126	Adhesion	—	—	Stable
4a-h2	8.1	5.3	0.2	Unstable	0.334	0.85	0.253	0.00151	Unstable
4b-h2	8.1	5.3	0.4	Stable	0.334	Adhesion	—	—	Stable
5a-W1	8	5.3	0.2	Dripping	0.341	0.84	0.111	0.001	Unstable
5b-W1	8	5.3	0.4	Stable	0.341	Adhesion	—	—	Stable
5c-W1	8	5.3	0.8	Stable	0.341	Adhesion	—	—	Stable
5a-W2	4	5.3	0.2	Dripping	0.845	0.620	0.204	0.00339	Unstable
5b-W2	4	5.3	0.4	Dripping	0.845	0.789	0.253	0.00516	Unstable
5c-W2	4	5.3	0.8	Stable	0.845	0.983	0.326	0.00859	Stable

and 9. As mentioned in the previous section, the nonadhering configuration or the adhering one is established depending on whether that flow rate ratio is reached by increasing or decreasing the jet flow rate, respectively. As can be observed, the fact that the jet touches the wall stabilizes the basic flow for all the Reynolds and Weber numbers considered. Therefore, either stable or unstable experimental realizations can be produced depending on how the flow rate ratio is imposed.

The magnitude of the damping factor in Fig. 14 generally increases as the Weber number decreases for the range of wave numbers considered. This implies that the surface tension plays a stabilizing role in the evolution of most dominant modes, as occurs in the bending oscillations of jets [28]. Figure 15 shows the complex dependence of the dominant mode damping factor on the Reynolds number (the jet viscosity). The magnitude of the damping factor either increases or decreases as the viscosity increases depending on both the wave number and the Reynolds number.

IV. COMPARISON WITH EXPERIMENTS

In this section, we analyze the experimental results presented by Humphry *et al.* [20] in terms of our stability analysis. In that work, the authors claimed that noncylindrical jets were observed in many experiments, which would imply that the flow was not fully developed (parallel) in those realizations. It is also possible that the jet adhered to the wall in some cases, something difficult to determine from the images acquired in the experiments. Table I shows the results for the cases considered in Figs. 4 and 5 of Ref. [20]. In these cases, the data necessary to carry out the numerical study is available. Specifically, we calculate the value of $\mathcal{R}$ as that leading to the experimental value of the flow rate ratio. In addition, the Reynolds and Weber numbers are estimated by assuming $\rho_1 = \rho_2 = 10^3$ kg/m^3.

As can be observed, the experimental configuration became stable when the flow rate ratio was increased. Either dripping or unstable jetting gave rise to stable jetting for sufficiently large values of Q. If one leaves aside the question of whether the jet touches the channel wall or not, there is complete agreement between the outcome in the experiments and the predictions of the linear stability analysis. According to our calculations, the last case of the table corresponds to a jet stabilized by the channel wall without touching it. Figure 16 shows the dominant growth rate for the cases 5a-W2, 5b-W2, and 5c-W2. As can be observed, viscous stresses manage to stabilize the jet for $Q = 0.8$ ($\mathcal{R} = 0.983$) even though the jet does not touch the wall in this case. Stabilization is achieved for a Weber number of the order of 10^{-2}, which reveals the strong effect of confinement on the evolution of small-amplitude perturbations.

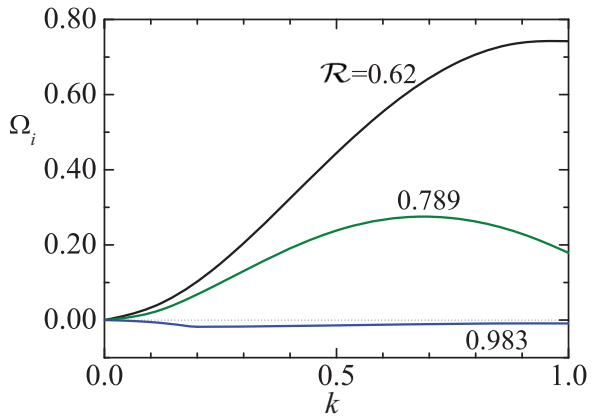

FIG. 16. Growth rate Ω_i of the dominant mode as function of the wave number k for the cases 5a-W2, 5b-W2, and 5c-W2 in Table I.

V. CONCLUSIONS

We analyzed the base flow and linear stability of a jet flowing in a rectangular microchannel both when the jet does not touch the solid surfaces and when it adheres to them with contact angles slightly smaller than 180°. For small values of the viscosity ratio μ, there is a range of the flow rate ratio, $Q_{\min} \leqslant Q \leqslant Q_{\max}$, for which the jet moves freely or adheres to the channel walls depending on whether the flow was established by increasing or decreasing the value of Q. The difference $Q_{\max} - Q_{\min}$ increases as the viscosity ratio decreases and the channel aspect ratio increases. Viscous stresses in the thin layer enclosed by the channel wall and the interface can completely stabilize the jet for sufficiently high viscosities or low-enough surface tensions. When the jet adheres to the channel walls, the growth of the dominant capillary mode is fully supressed and the flow becomes stable. These results allow us to conclude that, under certain parameter conditions, linearly stable or unstable experimental realizations can be produced depending on how the flow rate ratio is established. Specifically, stable jets can be obtained if the experimenter reduces progressively the jet flow rate while keeping constant that of the outer stream, while instability arises in the opposite case.

Our work mainly addresses the question of whether all infinitesimal perturbations naturally arising in a capillary jet can be damped out by confining it in a microchannel. This question cannot be easily addressed experimentally for several reasons. Perturbations growing at very slow rates are very difficult to detect. The critical conditions correspond to very small distances between the interface and the channel wall. Determining whether the jet touches the wall or not under those conditions is not an easy task. When a perturbation grows, its amplitude may become comparable with the interface-to-wall distance at the early stage of the perturbation growth, which implies that finite-amplitude effects may come into play when the perturbation is hardly detectable. These effects may stabilize the system, which would make linearly unstable jets appear as stable ones.

Our results are consistent with the experiments conducted by Humphry *et al.* [20], who produced jets that steadily flowed across channels without breaking up into droplets. If one leaves aside the question of whether the jet touches the channel wall or not, then there is complete agreement between the outcome in the experiments considered and the predictions of our linear stability analysis.

Based on our results, one is tempted to propose the Ohnesorge number $\widetilde{\mathrm{Oh}} = \mu_2(\rho_1\sigma\mathcal{R})^{-1/2}$ as the critical parameter to determine whether a confined jet is linearly stable or not.

Sepecifically, stability can be reached for sufficiently large values of that parameter. The critical Ohnesorge number $\widetilde{\mathrm{Oh}}_c(\omega, \mathcal{R}, \rho, \mu, \mathrm{Re}, \mathrm{We})$ could be calculated by using the long wave approximation to determine the parameter conditions for which $\partial\Omega_i/\partial k|_{k=0}$ becomes negative, and, therefore, the system becomes stable.

ACKNOWLEDGMENTS

Partial support from the Ministerio de Economía y Competitividad and Junta de Extremadura (Spain) through Grants No. DPI2016-78887 and No. GR18175, respectively, is gratefully acknowledged.

[1] R. Seemann, M. Brinkmann, T. Pfohl, and S. Herminghaus, Droplet based microfluidics, Rep. Prog. Phys. **75**, 016601 (2012).

[2] K. B. Migler, String Formation in Sheared Polymer Blends: Coalescence, Breakup, and Finite Size Effects, Phys. Rev. Lett. **86**, 1023 (2001).

[3] F. Savart, Mémoire sur la constitution des veines liquides lancées par des orifices circulaires en mince paroi, Ann. Chim. Phys. **53**, 337 (1833).

[4] J. A. F. Plateau, *Statique Expérimentale et Théorique des Liquides Soumis Aux Seules Forces Moléculaires* (Gauthier-Villars, Paris, 1873).

[5] L. Rayleigh, On the instability of jets, Proc. Lond. Math. Soc. **s1-10**, 4 (1878).

[6] S. Tomotika, Breaking up of a drop of viscous liquid immersed in another viscous fluid which is extending at a uniform rate, Proc. R. Soc. Lond. **153**, 302 (1936).

[7] C. E. Hickox, Instability due to density and viscosity stratification in an axisymmetric pipe flow, Phys. Fluids **14**, 251 (1971).

[8] P. Guillot, A. Colin, A. S. Utada, and A. Ajdari, Stability of a Jet in Confined Pressure-Driven Biphasic Flows at Low Reynolds Numbers, Phys. Rev. Lett. **99**, 104502 (2007).

[9] P. Guillot, A. Colin, and A. Ajdari, Stability of a jet in confined pressure-driven biphasic flows at low Reynolds number in various geometries, Phys. Rev. E **78**, 016307 (2008).

[10] P. J. A. Janssen, H. E. H. Meijer, and P. D. Anderson, Stability and breakup of confined threads, Phys. Fluids **24**, 012102 (2012).

[11] A. Frischknecht, Stability of cylindrical domains in phase-separating binary fluids in shear flow, Phys. Rev. E **58**, 3495 (1998).

[12] M. J. Russo and P. H. Steen, Shear stabilization of the capillary breakup of a cylindrical interface, Phys. Fluids A **1**, 1926 (1989).

[13] M. A. Herrada, A. S. Mohamed, J. M. Montanero, and A. M. Gañán-Calvo, Stability of a rivulet flowing in a microchannel, Int. J. Multiphase Flow **69**, 1 (2015).

[14] M. N. Kashid, W. Kowalinski, A. Renken, J. Baldyga, and L. Kiwi-Minsker, Analytical method to predict two-phase flow pattern in horizonta micro-capillaries, Chem. Eng. Sci. **74**, 219 (2012).

[15] C. Cramer, P. Fischer, and E. J. Windhab, Drop formation in a co-flowing ambient fluid, Chem. Eng. Sci. **59**, 3045 (2004).

[16] A. S. Utada, A. Fernandez-Nieves, H. A. Stone, and D. A. Weitz, Dripping to Jetting Transitions in Coflowing Liquid Streams, Phys. Rev. Lett. **99**, 094502 (2007).

[17] A. S. Utada, A. Fernandez-Nieves, J. M. Gordillo, and D. A. Weitz, Absolute Instability of a Liquid Jet in a Coflowing Stream, Phys. Rev. Lett. **100**, 014502 (2008).

[18] T. Cubaud and T. G. Mason, Capillary threads and viscous droplets in square microchannels, Phys. Fluids **20**, 053302 (2008).

[19] S. D. Geschiere, I. Ziemecka, V. van Steijn, G. J. M. Koper, J. H. van Esch, and M. T. Kreutzer, Slow growth of the Rayleigh-Plateau instability in aqueous two phase systems, Biomicrofluidics **6**, 022007 (2012).

[20] K. J. Humphry, A. Ajdari, A. Fernández-Nieves, H. A. Stone, and D. A Weitz, Suppression of instabilities in multiphase flow by geometric confinement, Phys. Rev. E **79**, 056310 (2009).

[21] M. R. de Saint Vincent, H. Chraibi, and J.-P. Delville, Optical Flow Focusing: Light-Induced Destabilization of Stable Liquid Threads, Phys. Rev. Appl. **4**, 044005 (2015).

[22] Y. Son, N. S. Martys, J. G. Hagedorn, and K. B. Migler, Suppression of capillary instability of a polymeric thread via parallel plate confinement, Macromolecules **36**, 5825 (2003).

[23] Z. Li, A. M. Leshansky, L. M. Pismen, and P. Tabeling, Step-emulsification in a microfluidic device, Lab Chip **15**, 1023 (2015).

[24] S. R. Hodges, O. E. Jensen, and J. M. Rallison, The motion of a viscous drop through a cylindrical tube, J. Fluid Mech. **501**, 279 (2004).

[25] E. B. Dussan, On the spreading of liquids on solid surfaces: Static and dynamic contact lines, Annu. Rev. Fluid Mech. **11**, 371 (1979).

[26] M. R. Khorrami, M. R. Malik, and R. L. Ash, Application of spectral collocation techniques to the stability of swirling flows, J. Comput. Phys. **81**, 206 (1989).

[27] M. A. Herrada and J. M. Montanero, A numerical method to study the dynamics of capillary fluid systems, J. Comput. Phys. **306**, 137 (2016).

[28] M. A. Herrada, J. M. Montanero, C. Ferrera, and A. M. Gañán-Calvo, Absolute lateral instability in capillary coflowing jets, Phys. Fluids **22**, 064104 (2010).